The Seasonal Variability of the Arctic Ocean Ekman Transport and Its Role in the Mixed Layer Heat and Salt Fluxes

JIAYAN YANG

Department of Physical Oceanography, Woods Hole Oceanographic Institution, Woods Hole, Massachusetts

(Manuscript received 28 June 2005, in final form 27 December 2005)

ABSTRACT

The oceanic Ekman transport and pumping are among the most important parameters in studying the ocean general circulation and its variability. Upwelling due to the Ekman transport divergence has been identified as a leading mechanism for the seasonal to interannual variability of the upper-ocean heat content in many parts of the World Ocean, especially along coasts and the equator. Meanwhile, the Ekman pumping is the primary mechanism that drives basin-scale circulations in subtropical and subpolar oceans. In those ice-free oceans, the Ekman transport and pumping rate are calculated using the surface wind stress. In the ice-covered Arctic Ocean, the surface momentum flux comes from both air–water and ice–water stresses. The data required to compute these stresses are now available from satellite and buoy observations. But no basin-scale calculation of the Ekman transport in the Arctic Ocean has been done to date. In this study, a suite of satellite and buoy observations of ice motion, ice concentration, surface wind, etc., will be used to calculate the daily Ekman transport over the whole Arctic Ocean from 1978 to 2003 on a 25-km resolution. The seasonal variability and its relationship to the surface forcing fields will be examined. Meanwhile, the contribution of the Ekman transport to the seasonal fluxes of heat and salt to the Arctic Ocean mixed layer will be discussed. It was found that the greatest seasonal variations of Ekman transports of heat and salt occur in the southern Beaufort Sea in the fall and early winter when a strong anticyclonic wind and ice motion are present. The Ekman pumping velocity in the interior Beaufort Sea reaches as high as 10 cm day^{-1} in November while coastal upwelling is even stronger. The contributions of the Ekman transport to the heat and salt flux in the mixed layer are also considerable in the region.

1. Introduction

The late-summer sea ice concentration in the Arctic Ocean, according to remote sensing data, has been decreased at a rate of about 3% $decade^{-1}$ since mid-1970s when satellite passive microwave sensors started to provide the basinwide observation of the global sea ice coverage (Parkinson et al. 1999). While the long-term variability of ice volume is not yet clear, some studies have nevertheless indicated that sea ice has also been thinning (Rothrock et al. 1999). The heat content in the oceanic mixed layer directly influences the water–ice heat flux and thus is considered to be a leading factor that determines the state of the Arctic sea ice. Processes that govern the heat-content variability in the upper Arctic Ocean have not been sufficiently investigated because of the severe scarcity of the Arctic oceanographic observations. Assumptions have often been made mainly based on indirect observations. The oceanic heat flux to the ice in the central Arctic, estimated to be around about 2 W m^{-2}, has been shown to be required in order to simulate the observed thickness of perennial ice (Maykut and Untersteiner 1971). Because of the insulation of a very stable Arctic halocline, which is replenished by water formed in the shelf regions (Aagaard et al. 1981), a major source of heat flux is likely the solar radiation to the oceanic mixed layer through open leads and thin ice (Maykut and McPhee 1995; Maykut and Perovich 1987). But how this heat flux is redistributed by oceanic currents has been less studied.

In the summer, there are usually large areas of open water or thin-ice covering along the Arctic boundaries. The water temperature in the mixed layer in those areas is usually considerably higher than the freezing point because of both an enhanced solar radiation associated with a lower albedo and the influence of

Corresponding author address: Jiayan Yang, Dept. of Physical Oceanography, Woods Hole Oceanographic Institution, Woods Hole, MA 02543.
E-mail: jyang@whoi.edu

warmer Pacific and Atlantic waters that tend to flow along the boundary after entering the Arctic basin. How can the large amount of heat stored in those areas be released or redistributed? Will intense cooling from the atmosphere in the following fall and winter remove the heat locally from the ocean or will advection transport it elsewhere to remotely influence the ice condition there? To address these issues, it is important to understand how the Arctic Ocean responds to the atmosphere–ice forcing. From the perspective of physical oceanography, the Ekman-layer transport is perhaps the most fundamental field from where a more complicated three-dimensional circulation structure can be examined.

The stress that acts on the surface of the ice-covered Arctic Ocean is due to both wind and ice motion. Before the satellite remote sensing era, the ice motion data in the Arctic had been inferred from geostrophic wind (Colony and Thorndike 1984) or from positioning a number of sparsely distributed drifting buoys (Rigor 2002). A lack of high-resolution and good-quality data of ice motion is perhaps a leading reason for why previous calculations of Ekman velocity and pumping rate were limited in the ice-free oceans (i.e., Hellerman and Rosenstein 1983). This situation has been changed recently due to the new capability of retrieving ice motion information from satellite passive microwave data (Kwok et al. 1998; Fowler 2003). Using these newly available ice motion data, we can now calculate the basinwide Ekman transport and pumping rate and estimate their contributions to the heat and freshwater fluxes. This study attempts to examine the role of Ekman transport in the seasonal variability of the mixed-layer heat and salt fluxes. Higher-order dynamic oceanic processes, such as the geostrophic transport, will be left for future studies. Without comprehensive oceanographic data, the three-dimensional circulation field can only be dealt with by using ocean general circulation models and such efforts have already been made (e.g., Zhang et al. 1998; Zhang and Hunke 2001; Maslowski et al. 2000; Proshutinsky et al. 2001; Hakkinen and Proshutinsky 2004).

In this study, a suite of data, including the sea level pressure (SLP), geostrophic wind, sea ice concentration, sea ice motion, and the temperature and salinity in the upper Arctic Ocean, are used. We will concentrate on the seasonal time scale. Interannual variations of the Ekman transport and pumping rate will be addressed in future studies. Long-term variability of some atmosphere and sea ice variables used in this study has been addressed in previous studies (e.g., Walsh et al. 1996; Parkinson et al. 1999; Thompson and Wallace 1998; Proshutinsky and Johnson 1997; Dickson et al. 2000; Johnson et al. 1999; Comiso et al. 2003). The data sources will be described in section 2. The seasonal variability of each variable will be discussed. The calculation of the Ekman transport and Ekman pumping will be presented and discussed in section 3. In section 4, we will estimate the contributions from the Ekman dynamics to the heat and freshwater budgets in the upper Arctic Ocean. A summary and more detailed discussion will be followed in section 5.

2. The data sources and seasonal variability of atmospheric, ice, and oceanic variables

The seasonal variability of SLP, geostrophic wind, ice motion, ice concentration, and the upper-ocean temperature and salinity will be discussed in this section. We would like to point out that each variable is discreted in different grid format, and so the first step we took was to linearly interpolate all variables into a common grid, a 25-km grid used in the ice motion vectors (Fowler 2003). The domain of this study is shown in Fig. 1 with land marked by in white and the ocean in gray. A grid is assigned to be a land value if it happens to be a land grid in any of the variables (i.e., SLP, ice motion, ice concentration, temperature, and salinity). In other words, the land mask shown in Fig. 1 is a stacked one, which is why the land–sea boundary shape is not well defined in many areas.

a. SLP and geostrophic wind vectors

In the study, the twice daily SLP data from the International Arctic Buoy Program (IABP; Rigor 2002), which has a resolution of 2° in latitude and 10° in longitude, are interpolated into the common grid. The regridded SLP is used to compute the daily geostrophic wind vector (u_g, v_g). The 26-yr averaged monthly climatology (Fig. 2) shows that SLP weakens in the summer with a minimum around July–August. The geostrophic wind then becomes cyclonic in the central Arctic Ocean from June to September. In September–October, the low SLP center retreats southward to the Nordic Seas and a high one appears in the central Arctic. The high SLP center continues to intensify and reaches its maximum state in March–April. Because of the presence of this high pressure center, an anticyclonic wind persists through this period. The high SLP recedes rapidly after April and by the early summer (June), the high center is much weakened and moves to the south Beaufort Sea area. The change of SLP between the maximum in April and minimum in August is about 20 mb. It is interesting to note that the strength of the anticyclonic wind over the Arctic Ocean is weaker

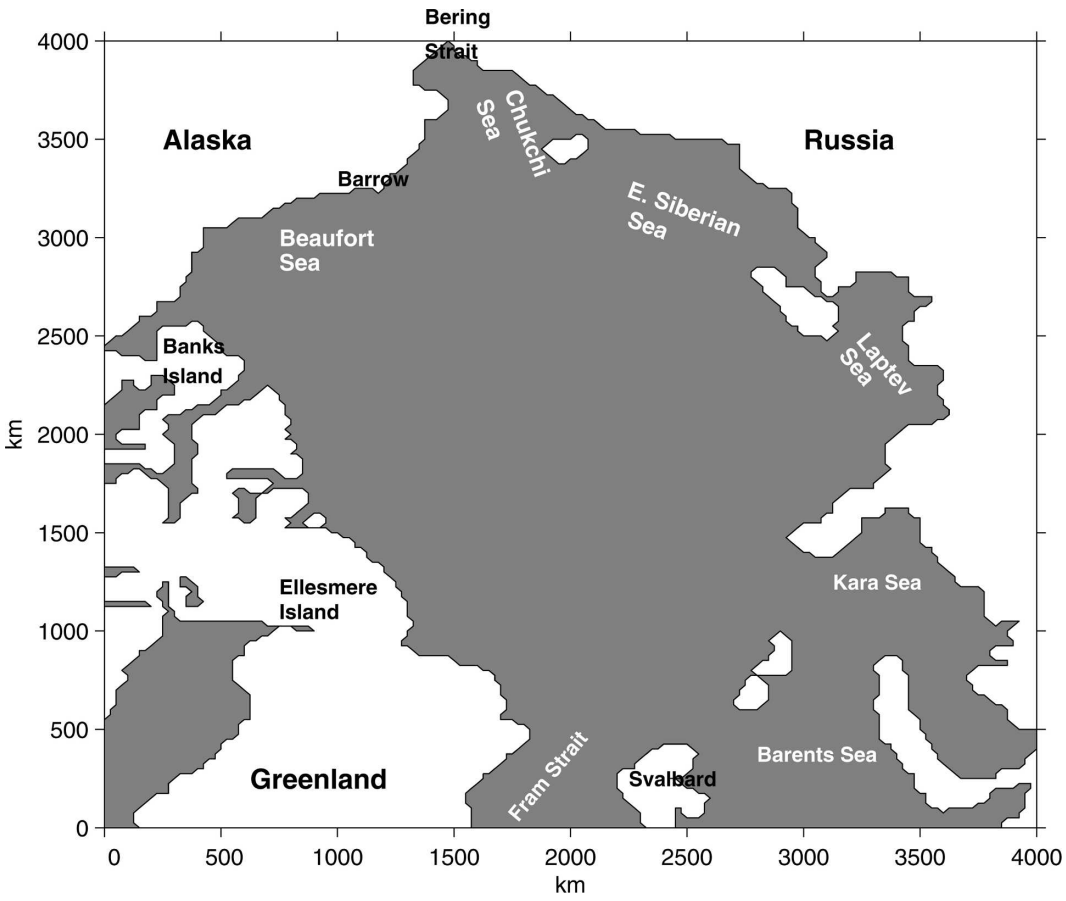

FIG. 1. The model domain. The land mask is a stacked one with four types of data (ice concentration, motion, SLP, and hydrography), and that is why the land–sea boundary is not well defined.

in January–March than in November–December even though the SLP has strengthened over this period. The high SLP center is moved toward Siberia and the SLP contours become more belt-shaped along x direction, particularly in January and February, resulting in a weaker anticyclonic wind. This structure modification will result in a coherent change in the sea ice motion as to be shown later. The high SLP center moves back to the central Arctic in April and to the Canadian basin in May, resulting in the second seasonal peak of the anticyclonic geostrophic wind and the ice motion (to be shown later). Since the anticyclonic wind is stronger and lasts for a longer period, the annual mean of geostrophic wind is anticyclonic (not shown here).

As to be discussed later, the seasonal reversal of the wind to a cyclonic one in the summer has a considerable impact on the upwelling field, especially in the southern Beaufort Sea. Yang and Comiso (2005) suggested that this seasonal variability was most likely responsible for the unexpected seasonal salinity variations, high in the summer and low in the winter, observed by Ice–Ocean Environmental Buoys in late 1990s in the upper Beaufort Sea.

We would like to point out explicitly here that the surface wind stress used in our Ekman-layer calculation, to be shown in section 3, is not based on the monthly wind climatology shown in Fig. 2. We calculated the daily wind stress from 1978 to 2003, which is then used to compute the 26-yr averaged daily climatology. If we had used the climatological wind, shown in Fig. 2, to calculate the stress, the magnitude would have been underestimated because of the nonlinear relationship between stress and wind speed (to be discussed in section 3).

b. Sea ice motion vectors

Sea ice in the Arctic Ocean moves constantly in response to air–ice and to water–ice stresses exerted by wind and oceanic current. The monthly climatology, shown in Fig. 3, is derived from a 26-yr daily record which is computed from using the Scanning Multichannel Microwave Radiometer (SMMR), Special Sensor

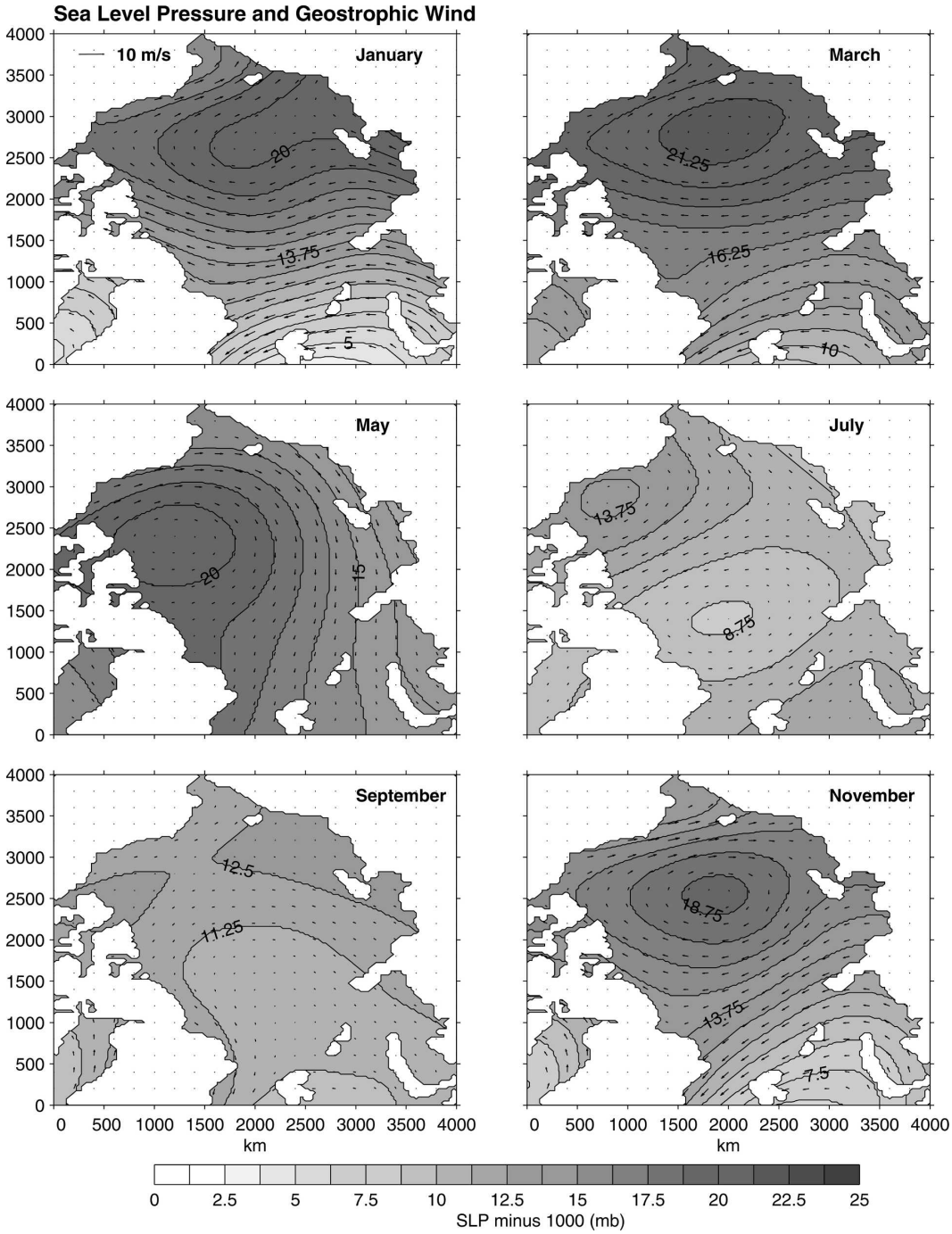

FIG. 2. Sea level pressure and geostrophic wind vectors from the International Arctic Buoy Program (Rigor 2002). The climatology is based on the 26-yr twice-daily data from 1978 to 2003.

Microwave Imager (SSM/I), Advanced Very High Resolution Radiometer (AVHRR), and buoy data (Fowler 2003). The seasonal variability of the ice motion reflects that in the surface wind field. As shown in Fig. 2, the geostrophic wind turns anticyclonic in September and sea ice responds to this change. The anticyclonic motion of sea ice starts to intensify in September in the southern Beaufort Sea, and intensifies between October and December. It weakens, though remains anticyclonic, in February and March. This temporal weakening is due to the similar change in the geostrophic wind when the high SLP center moves to-

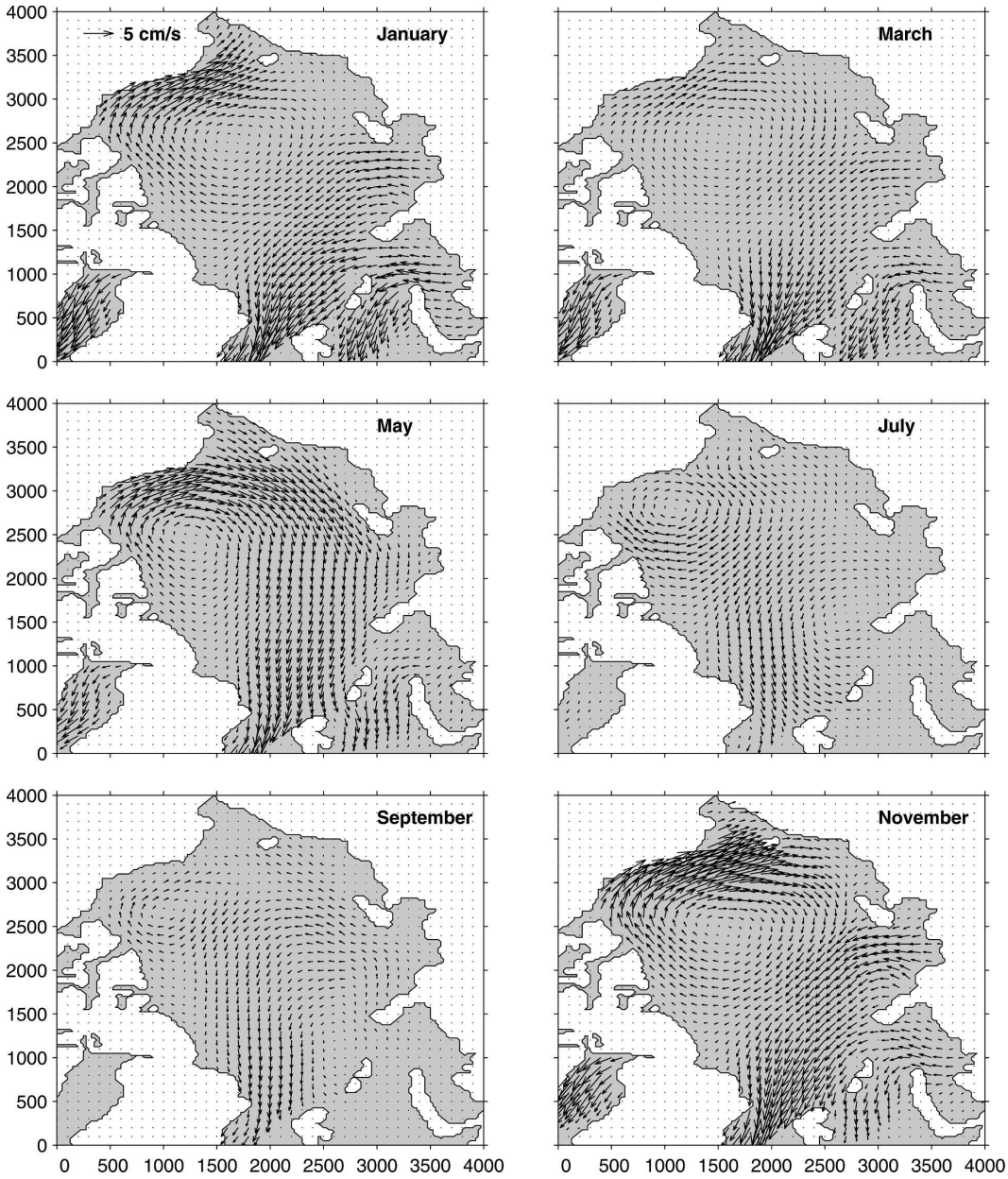

FIG. 3. The 26-yr (1978–2003) averaged monthly climatology of the ice motion. The ice motion vectors were derived from satellite passive microwave and AVHRR data and buoy observations (Fowler 2003). The daily field with a spatial resolution of 25 km is used to compute the monthly climatology.

ward the Siberia coast (Fig. 2). When the geostrophic wind intensifies again in April and May, the anticyclonic sea ice motion strengthens. In the summer, the anticyclonic motion weakens and retreats to the Beaufort Sea area. A cyclonic pattern is visible in the Eurasian Basin in July and August. Overall, the greatest seasonal change occurs in the southern Beaufort Sea along the Alaskan coast and in the areas to the north of Fram Strait. Although the typical ice motion speed shown in this climatology is less than 10 cm s^{-1}, the ice actually moves much faster in a typical daily field. The ice motion, like the wind field, changes rapidly in short time scales. The whole basin-scale motion pattern can be reversed within a month. For instance, strong cyclonic patterns of ice motion were observed in several winters although climatology indicates that the motion should be strongly anticyclonic. Like in the previous subsection with wind field, the ice–water stress used in

this study is calculated from the daily ice motion data instead of from the climatologic ice motion data shown in Fig. 3.

c. The sea ice concentration

The sea ice concentration over the whole Arctic basin has been well observed by satellite passive microwave sensors since mid 1970s (Comiso 1995), and so its seasonal and interannual variability over this period has been well documented (e.g., Parkinson and Cavalieri 1989; Gloerson et al. 1992) and thus will not be discussed further here. In our calculation, the sea ice concentration is used to partition the air–water and ice–water stresses in each grid. In the long winter season, the Arctic Ocean is covered almost completely by sea ice so that the surface stress is determined largely by ice motion data. In the summer and fall, sea ice concentration becomes lower, particularly in the coastal regions. We used the daily 25-km sea ice concentration data that were derived by using the bootstrap technique (Comiso 1995) from 1978 to 2003. A monthly climatology is created by averaging data in each month over the whole 26-yr data period (Fig. 4).

d. The upper-ocean salinity and temperature

To estimate the contributions from the Ekman transport to the salt and heat budgets in the Arctic Ocean mixed layer, we use the monthly data of temperature and salinity from the Polar Science Center's Hydrography Climatology (PHC; Steele et al. 2001). Few observations of velocity profiles are available in the Arctic Ocean, but a rare set of direct measurements of the Ekman spiral indicates that the depth of the frictional influence is about 20 m (Hunkins 1966). Therefore, we assume in this study a basinwide uniform depth of 20 m for the Ekman layer. We are fully aware that this depth should vary regionally depending on the latitude and vertical mixing processes. The salinity and potential temperature averaged in the upper 20 m will be used to represent their distributions in the Ekman layer.

The monthly salinity field, shown in Fig. 5, reveals a basin distribution that can be characterized by the high salinity in regions to the north of the Nordic Seas where the influence from the inflow of the high-salinity Atlantic water is evident. Away from Fram Strait and Barents Sea, the influence of the Atlantic water wanes and the salinity gradually decreases. The salinity is particularly low along the Canadian/Alaskan and Siberian coasts where river runoffs are a major source of freshwater. In the interior Arctic Ocean, there is a low salinity center in the Beaufort Sea, with S_{mix} ranging from 30 to 30.5 psu. This is associated with the anticyclonic Beaufort Gyre driven by the Ekman pumping. The seasonal change of S_{mix} in the interior is generally within 1 psu. But the variability in the coastal areas is much larger.

Because of the intense surface cooling in the winter season, the mixed layer temperature is near the freezing point and thus varies very little (Fig. 6). The coldest period appears to be in March–April when the whole basin is almost uniformly at the freezing point except in the eastern side of Fram Strait where the inflow of warmer Atlantic water is still visible. Starting in May and intensifying through the summer months, the coastal areas warm up gradually due to the solar radiation and to inflows of warmer waters from the Pacific and Atlantic Oceans.

The Arctic Ocean is known to have very shallow halocline (~50 m) and thermocline (~100 m) depths (Aagaard et al. 1981). Thus the vertical gradients of salinity and temperature are typically large as shown in Figs. 7 and 8 for the T and S differences between the mixed layer and at 30 m depth. The salinity is always higher at 30 m (with exceptions in some spotty areas) than in the mixed layer. The greatest difference occurs in the coastal areas and especially so in the summer months. The difference is greater than 2.5 psu in those areas. Such a large gradient is mainly due to the freshening associated with runoff and sea ice melting as reflected in the mixed layer salinity distribution, shown in Fig. 5. As we will show, the strong upwelling occurs also along the coasts, and thus this strong salinity gradient does contribute to a significant salt flux to the mixed layer in those regions. The vertical temperature gradient is nearly opposite to that of salinity (Fig. 8), with subsurface water at 30 m being generally cooler than that in the surface layer. Like in the salinity case, the largest temperature gradient occurs also along the coast. This is due to the warming of the mixed layer in the summer (Fig. 6) when sea ice cover retreats and the solar radiation increases.

3. The Arctic Ocean Ekman transport and upwelling field

The Arctic Ocean Ekman layer is forced by wind stress in the open-water areas and by ice–water stress in the ice-covered areas. The datasets described in section 2 are used here. All variables are daily and are interpolated into the common grid of 25-km resolution. The total stress in each grid is calculated by

$$\boldsymbol{\tau} = \alpha\boldsymbol{\tau}_{\text{ice}-\text{water}} + (1 - \alpha)\boldsymbol{\tau}_{\text{air}-\text{water}}, \tag{1}$$

where α is the fraction of the grid that is covered by sea ice, $\boldsymbol{\tau}_{\text{ice–water}}$ and $\boldsymbol{\tau}_{\text{air–water}}$ are the ice–water and air–

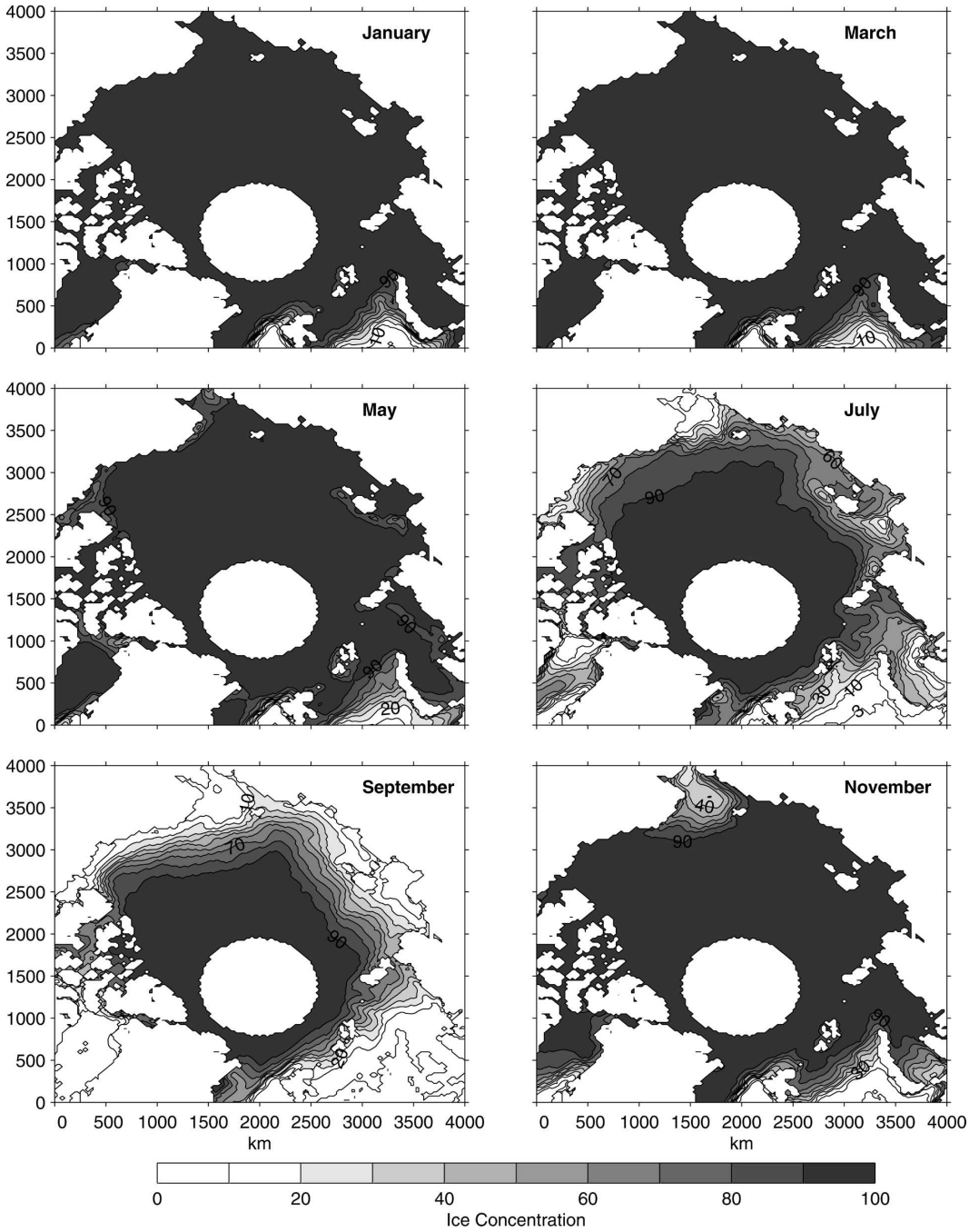

FIG. 4. The sea ice concentration (%) field from the satellite passive microwave data (Comiso 1995).

water interfacial stresses, respectively. The satellite passive microwave sea ice concentration data (Comiso 1995) is used for determining α.

The surface wind is needed for calculating the air–water stress. In this study, we follow the procedure adopted by the Arctic Ocean Model Intercomparison Project (AOMIP; Proshutinsky et al. 2001). The sea level pressure data are used to calculate the surface geostrophic wind, which is then converted to a 10-m surface wind by an empirical formula (Proshutinsky and Johnson 1997). Following the AOMIP procedure, the 10-m surface wind vector (u_s, v_s) is computed by using the following equations:

$$u_s = 0.8(u_g \cos 30^\circ - v_g \sin 30^\circ)$$
$$v_s = 0.8(u_g \cos 30^\circ + v_g \sin 30^\circ). \quad (2)$$

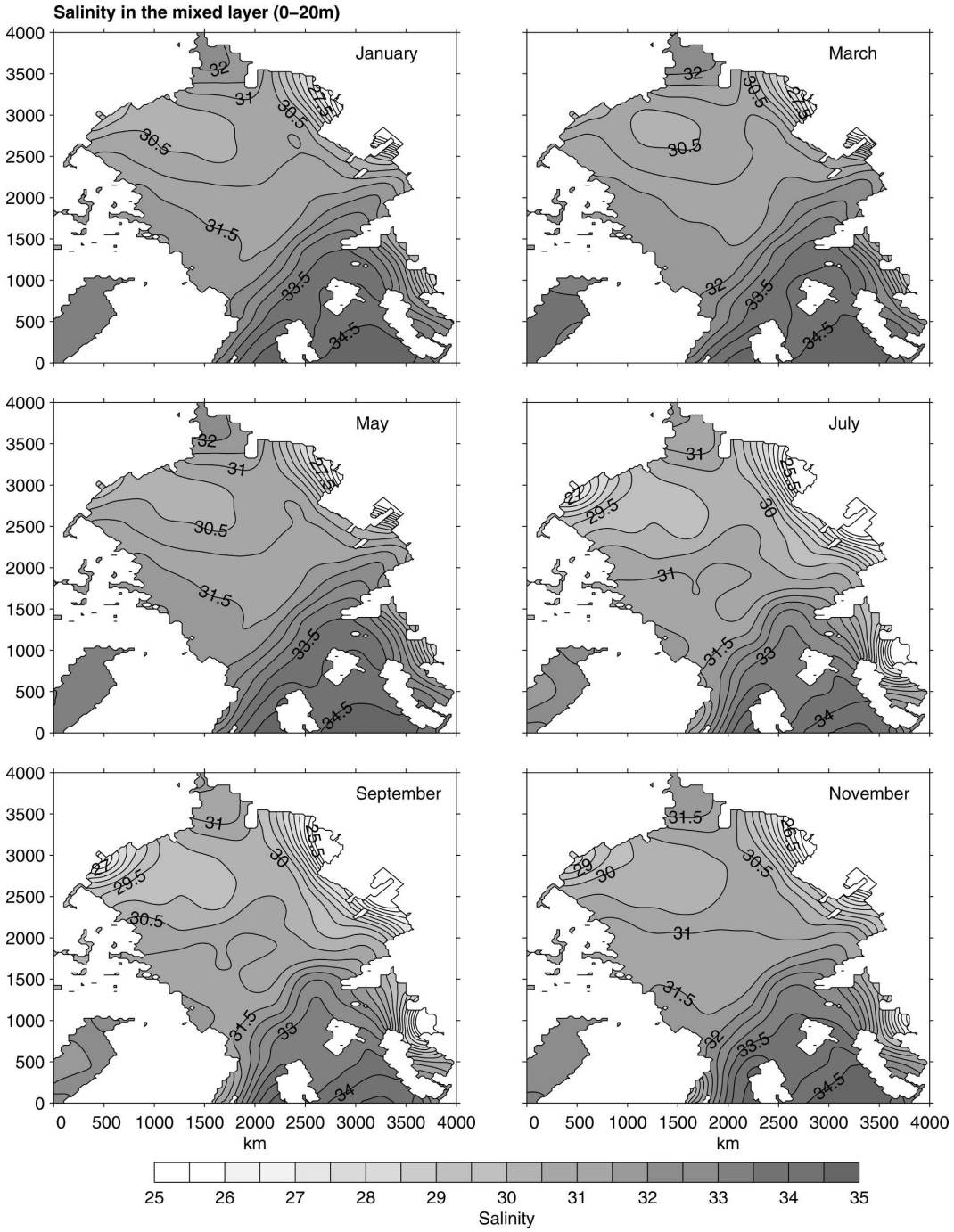

FIG. 5. The vertically averaged salinity (psu) in the upper 20 m, using the PHC climatology from Steele et al. (2001).

The air–water stress is then calculated from a bulk formula

$$\boldsymbol{\tau}_{\text{air}-\text{water}} = \rho_{\text{air}} C_d |\mathbf{u}_s| \mathbf{u}_s, \tag{3}$$

where $\rho_{\text{air}} = 1.25 \text{ kg m}^{-3}$ is the air density, $C_d = 0.001\,25$ is the drag coefficient.

The ice–water stress is computed by using the daily sea ice motion vectors (Fowler, 2003). The ice motion data were derived from using satellite (SMMR, SSM/I, AVHRR) and buoy observations. Again, we have followed the AOMIP procedure for the calculation the ice–water stress:

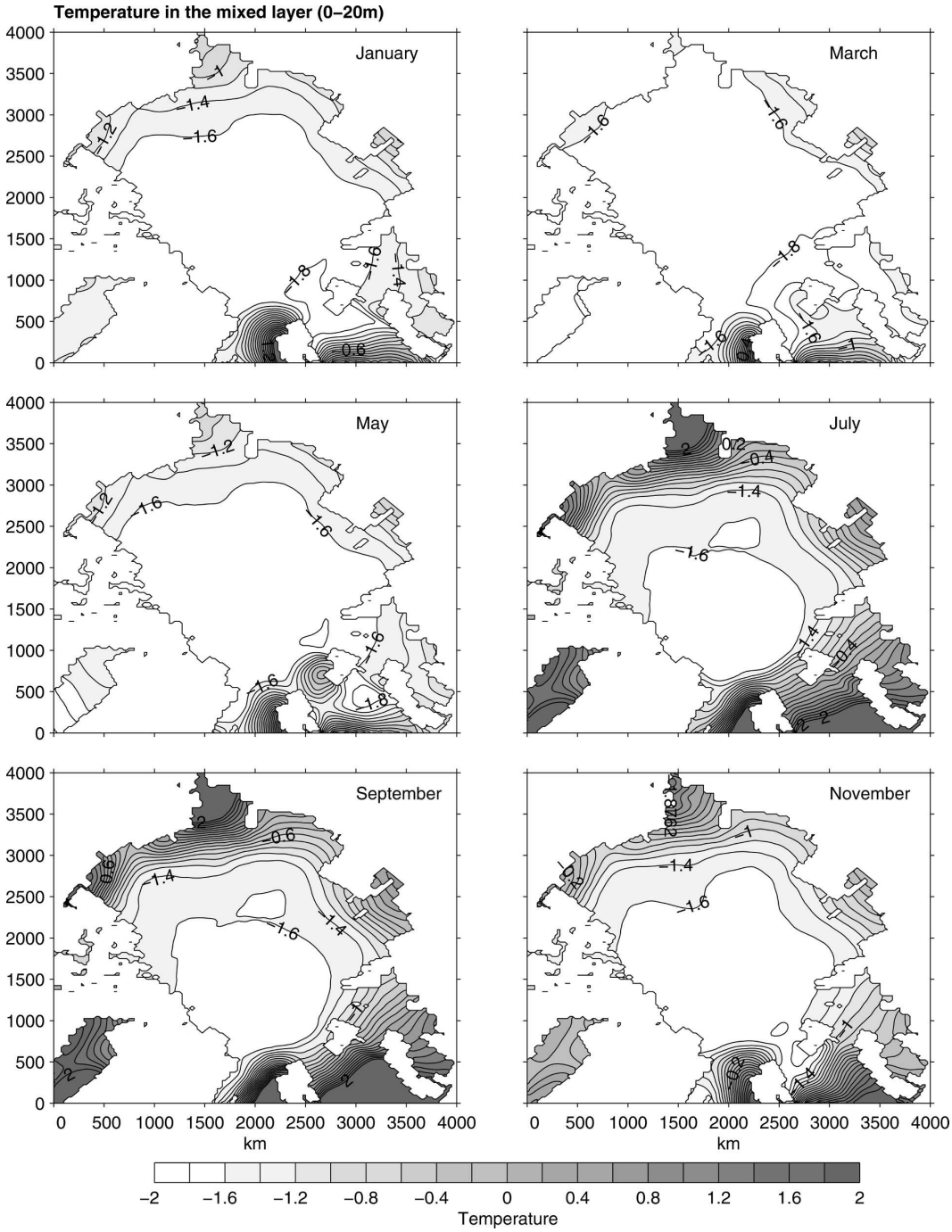

FIG. 6. The vertically averaged temperature (°C) in the upper 20 m, using the PHC climatology from Steele et al. (2001).

$$\boldsymbol{\tau}_{\text{ice}-\text{water}} = \rho_{\text{water}} C_{\text{iw}} |(\mathbf{u}_{\text{ice}} - \mathbf{u}_{\text{ocean}})| (\mathbf{u}_{\text{ice}} - \mathbf{u}_{\text{ocean}}), \tag{4}$$

where ρ_{water} is the water density, $C_{\text{iw}} = 0.0055$ is the ice–water drag coefficient (Hibler 1980), $\mathbf{u}_{\text{ice}}$ is the ice motion vector from Fowler (2003), and $\mathbf{u}_{\text{ocean}}$ is the upper-layer ocean current velocity for which the Ekman velocity $\mathbf{u}_{\text{Ekman}}$ is used. We must point out that neglecting the geostrophic velocity can induce considerable errors. Although geostrophic velocity is usually considered to be much smaller than ice drifting speed, it can be large along the coast, in fronts, and in Fram

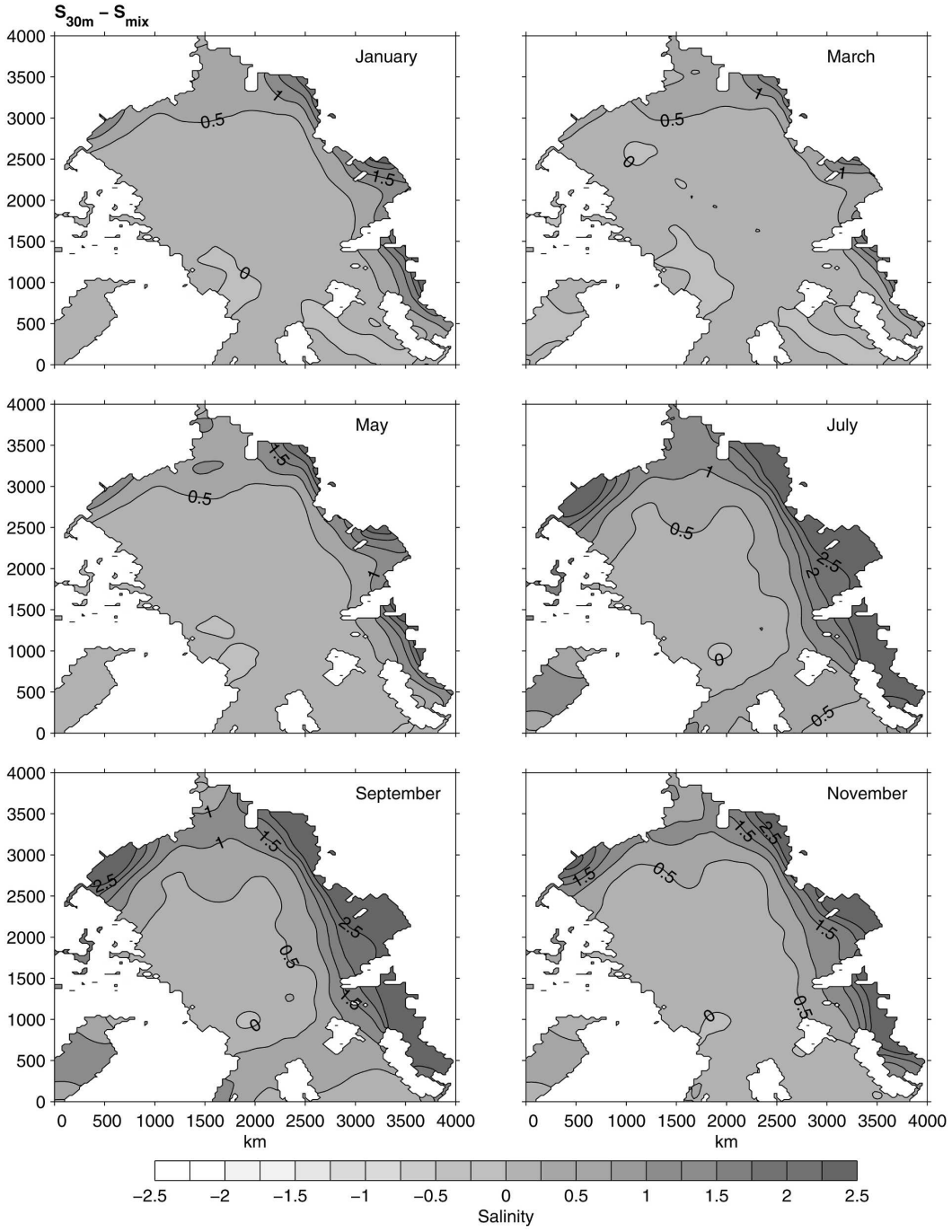

FIG. 7. The salinity (psu) difference between $z = -30$ m and the mixed layer (from PHC climatology; Steele et al. 2001).

Strait. In these regions, our calculation can be very biased.

With all those data, we can now calculate the Ekman layer velocity by using the textbook Ekman layer equation (e.g., Pond and Pickard 1983):

$$-fv_{\text{Ekman}} = \frac{\tau^x}{\rho D_E} \quad \text{and} \quad fu_{\text{Ekman}} = \frac{\tau^y}{\rho D_E}, \qquad (5)$$

where $D_E = 20$ m is the Ekman layer depth [the Arctic Ocean Ekman depth, according to observation by

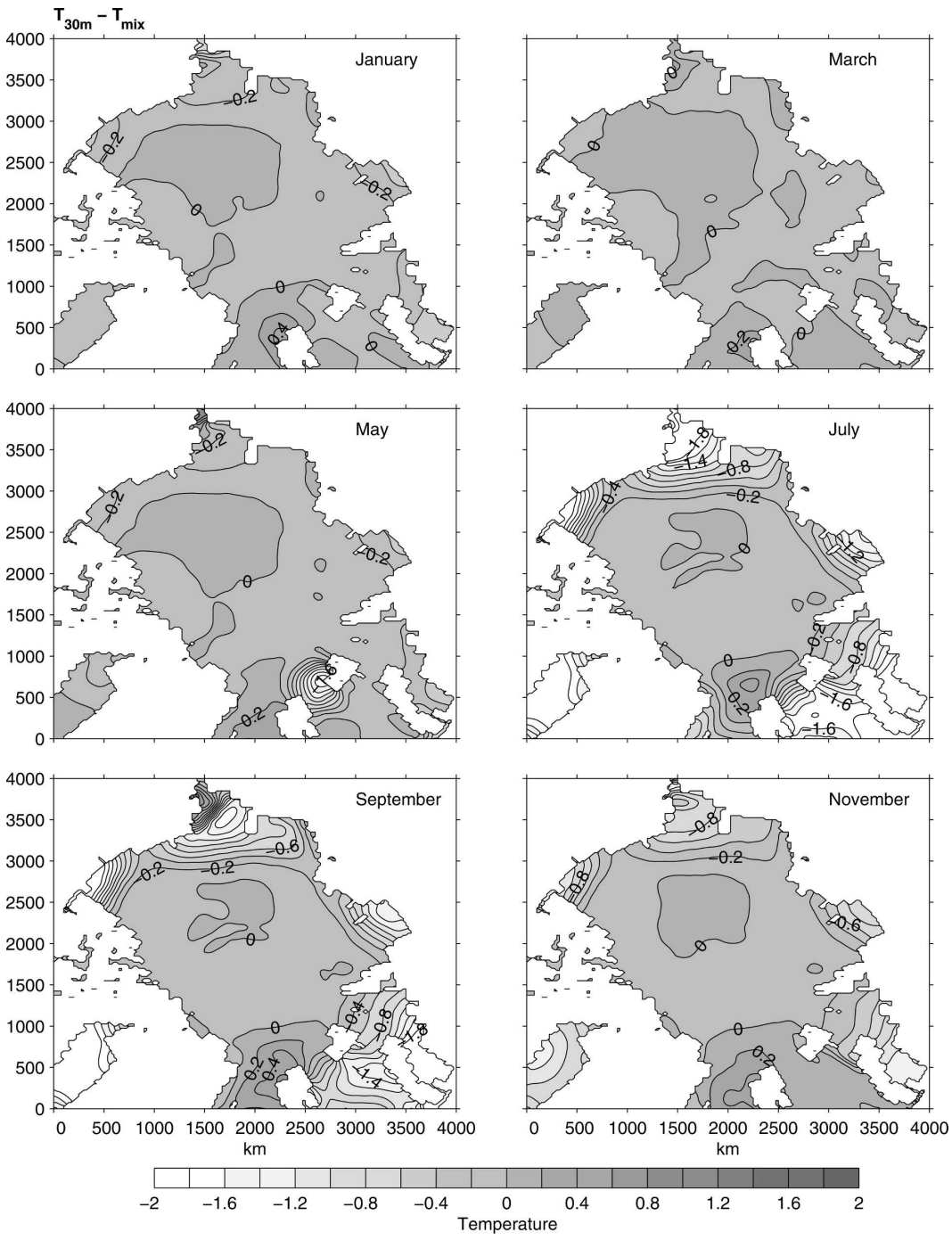

FIG. 8. The temperature (°C) difference between $z = -30$ m and the mixed layer. Note that the subsurface temperature at 30 m depth is lower in the coastal areas, especially in the summer. (Data from the PHC climatology; Steele et al. 2001).

Hunkins (1966), is about 18 m]. The Ekman velocity $(u_{\text{Ekman}}, v_{\text{Ekman}})$ in (5) is the vertically averaged velocity within the Ekman layer. Since the stress and the Ekman velocity are dependent on each other, Eqs. (3)–(5) are solved iteratively.

Figure 9 shows the seasonal climatology of the Ekman transport velocity $D_E(u_{\text{Ekman}}, v_{\text{Ekman}})$. The seasonal variability reflects the surface forcing fields, the wind and ice motion. The wind (Fig. 2) and ice motion (Fig. 3) start their anticyclonic phases in September and

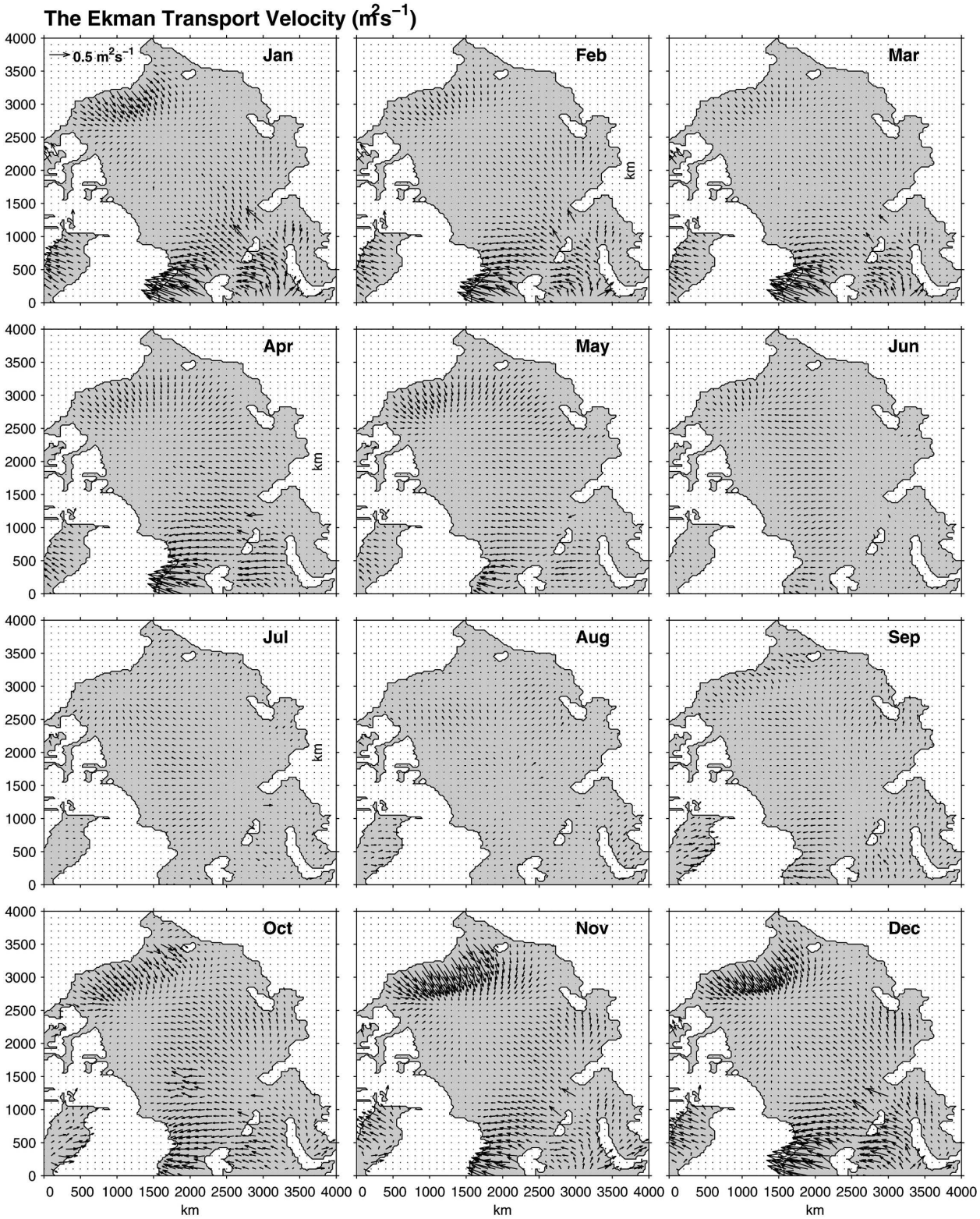

FIG. 9. The Ekman transport vector ($m^2\ s^{-1}$) computed by using (5). Note that there is a strong offshore transport in the Beaufort and Chukchi Seas in fall and early winter.

this transition leads to the development of the offshore Ekman transport in the fall and winter. The Ekman transport is particularly strong along the southern boundary in the Beaufort and Chukchi Seas. The offshore transport intensifies rapidly into the winter months, reaching the maximum in November and December. But even in these two months, the transport velocity is generally weaker than 1 $m^2 s^{-1}$ and so the depth-averaged Ekman velocity is less than 5 cm^{-1}. The Ekman transport in the Beaufort and Chukchi Seas weakens gradually from January to March.

Because of the migration of the high SLP center from Siberia to the Beaufort Sea, shown in Fig. 2 and discussed in section 2a, the pattern of the anticyclonic ice motion reintensified in April and May (Fig. 3). This resulted in a second peak of offshore Ekman transport in May not only along the southern Beaufort Sea boundary but also along Russian coast (Fig. 9). During the summer (June to August), both the surface wind and ice motion are weak. So the Ekman transport is also weak over the whole Arctic basin. Another area with a strong seasonal variation is within and to the north of Fram Strait. The Ekman transport in this region is typically westward. It becomes the strongest in the fall and winter just like in the Beaufort Sea. This westward Ekman flow is due to the strong southward ice transport (Fig. 3) directed toward the Nordic Seas and through Fram Strait.

Next, we will show w, the upwelling and downwelling field induced by the divergence and convergence of the Ekman transport. The distribution of w can be computed by

$$w = \nabla(D_E \mathbf{u}_{\text{Ekman}}). \quad (6)$$

In any land grid, the Ekman transport is set to be zero, and so there is usually a large convergence or divergence for any sea grid next to the land. The method used here is probably overly simplified for calculating coastal upwelling. For instance, it excludes the effect induced by remotely forced Kelvin waves. The method also becomes invalid in very shallow areas where the actual water depth is shallow than the Ekman depth (20 m used in this study). Nevertheless, the basinwide and daily upwelling field for a 26-yr period from 1978 to 2003 has been computed according to (6). The monthly climatology of w, shown in Fig. 10, is compiled by averaging the daily field in each month over this 26-yr period. The large area of white that is centered at the North Pole is due to the absence of sea ice concentration information from the SMMR data (SSM/I has a smaller area). The seasonal variability of w reflects the changes of the Ekman transport.

As shown in Fig. 9, the most prominent change of the Ekman velocity occurs in the Beaufort Sea, especially along the southern boundary. Starting in September, the Ekman transport starts to intensify in the southern Beaufort Sea. It is directed away from the Alaskan and Canadian coast toward the central Beaufort Sea. This offshore transport persists through the winter and spring, and peaks in a 4-month period from October to January. This leads to a strong Ekman convergence and thus downwelling in the Beaufort Sea and coastal upwelling along the boundary in these four months. The reintensification of the Ekman transport in April and May, as discussed in the previous section, results in the reappearance of strong downwelling in May (Fig. 10). The maximum downwelling rate in the interior Beaufort is about 15 cm day^{-1} in November and December. The coastal upwelling is restricted within a narrow zone along the boundary and the upwelling velocity is much larger than that of the interior downwelling. During the summer months, the interior Beaufort Sea is still dominated by downwelling although w is very weak, less than 5 cm day^{-1}. The seasonal variability of w in the eastern Arctic Ocean is not as well organized and also is considerably weaker except in the Laptev Sea.

Another area that shows a great seasonal variability is along Fram Strait. There is a strong westward Ekman transport from Svalbard toward Greenland between October and April. This transport is forced mainly by the strong southward sea ice motion associated with the Arctic sea ice export to the Nordic Seas. Consequently, upwelling dominates the eastern Fram Strait while downwelling persists off the Greenland's coast (Fig. 10). This contrast becomes the most striking in the winter months when the southward ice transport is the largest.

Several datasets have been used in the calculation of Ekman velocity and upwelling rate. The passive microwave data have a higher resolution than the IABP one and interpolation was used in order to merge them into a common grid. These procedures will inevitably induce errors, and may have contributed to spurious features seen in Fig. 10. In addition, it is well known that passive microwave sensors may underestimate the ice concentration in the summer season because of the presence of melt ponds. The discussion of the quality of each dataset can be found elsewhere in published literatures [e.g., Comiso (1995) for passive microwave data, and Rigor (2002) for the IABP data]. Here we will just present the standard error, calculated by using the 26-yr monthly upwelling rate (again the daily data were used to compile the month field in each individual year). Figure 11 shows that the standard error is generally much smaller than the monthly upwelling filed shown in Fig. 10. In Fram Strait and along the coastline, the

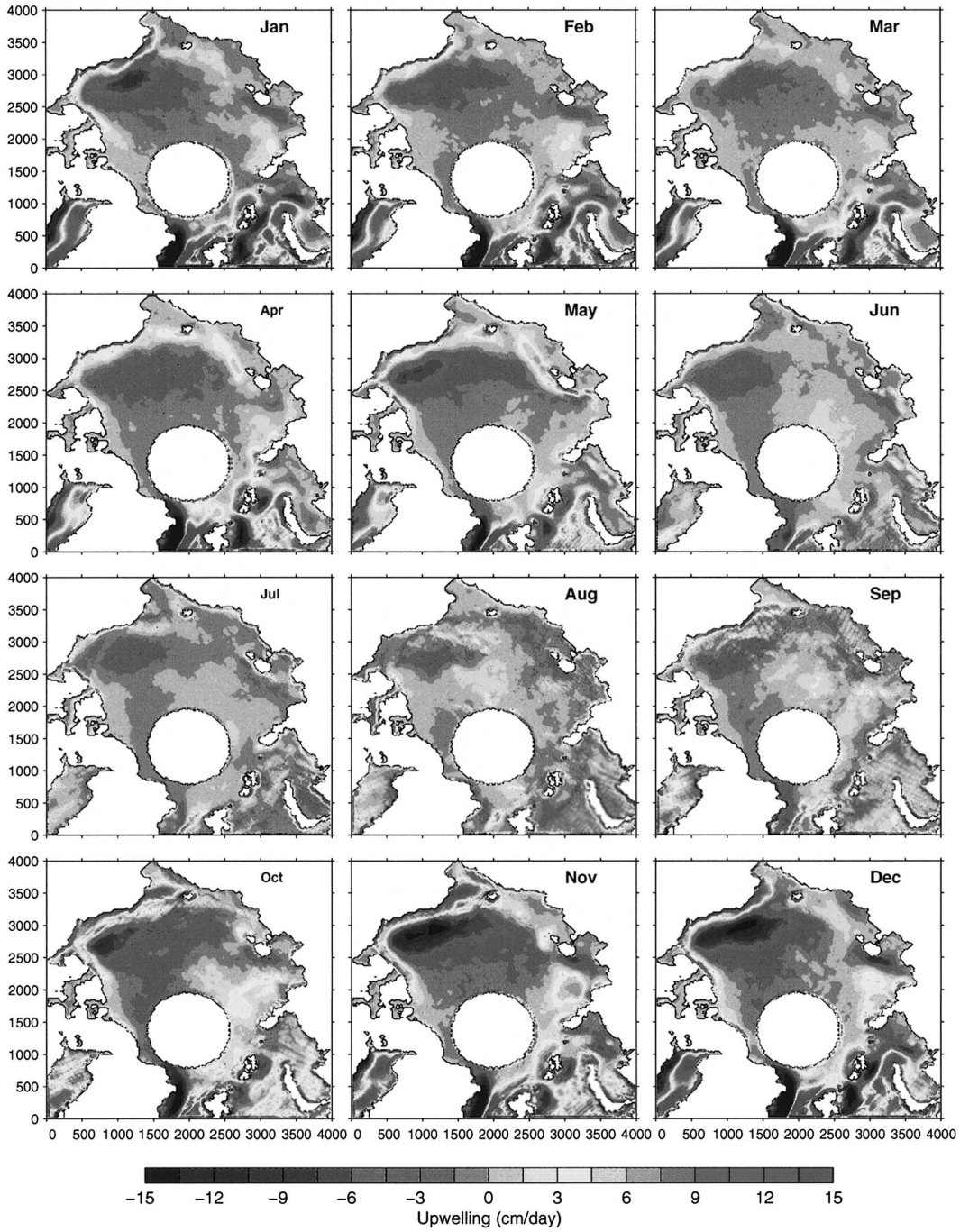

FIG. 10. The monthly upwelling rate (cm day^{-1}) computed from the divergence of the Ekman transport.

upwelling is strong and more variable, and the standard error is also larger in these areas.

4. The Ekman transport and heat and salt budget variability in the upper Arctic Ocean

The Ekman transport and its divergence, that is, upwelling rate, vary profoundly on the seasonal time scales. How this variability affects the heat and salt contents in the upper Arctic Ocean has seldom been examined, at least to the basin scale. The heat flux due to the horizontal advection is defined here by

$$Q_T^H = C_p \rho D_E (u_E \partial T/\partial x + v_E \partial T/\partial y), \quad (7)$$

where $C_p(T, S)$ is the specific heat that depends on the temperature and salinity. It is evaluated according to

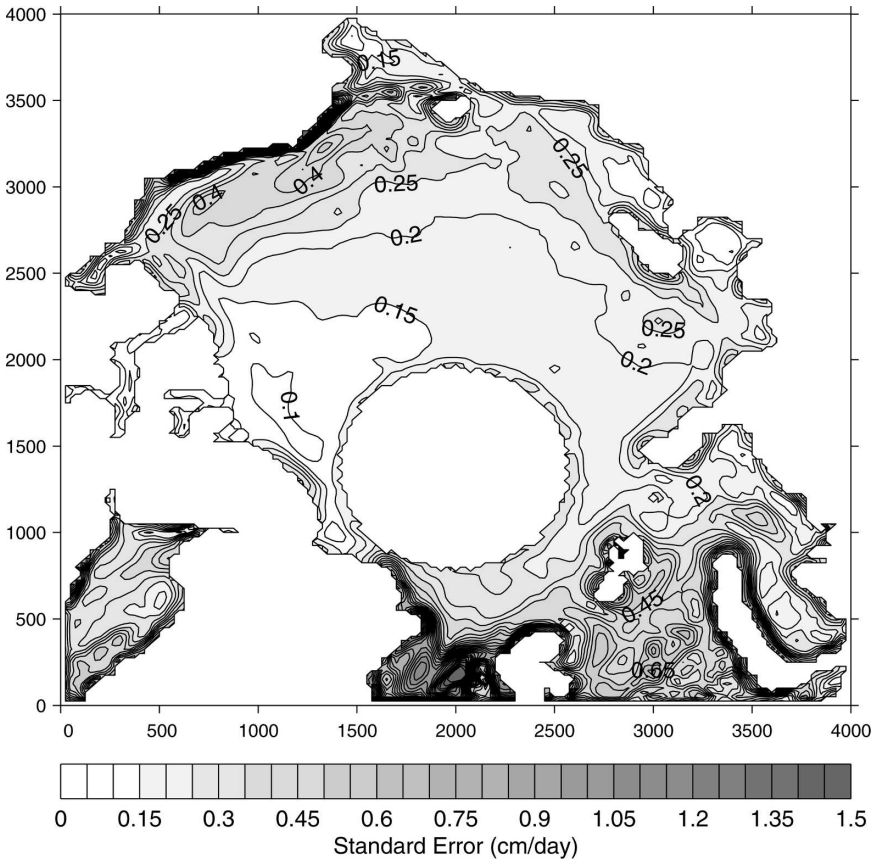

FIG. 11. The standard error (cm day^{-1}) for the upwelling calculation. Note the standard error is higher in the Fram Strait and along the coastline where the upwelling is stronger and more variable.

the formula given by Millero et al. (1973). The mean value is around 4000 J kg^{-1} K^{-1}.

In the lengthy winter season in the Arctic Ocean, the surface mixed layer temperature T_{mix} is uniformly cold at near freezing point T_f (Fig. 6) with small variations mainly due to the dependence of T_f on the salinity, which varies spatially in all seasons (Fig. 5). So the lateral gradient of T_{mix} is typically small through the whole winter and even in the spring. The contribution from the horizontal advection is small in the mixed-layer temperature. In summer, the enhanced heating from solar radiation in open water and low ice-covering areas, mostly in the coastal regions, and the inflows of warmer Pacific and Atlantic Waters through Bering and Fram Straits and through Barents Sea create large gradients in some coast regions (Fig. 6). The most pronounced contribution from Ekman advection occurs in the southern Beaufort and Chukchi Seas in the fall season. As we have discussed before, the anticyclonic wind and ice motion starts in September which drives a strong offshore Ekman transport. This strong Ekman transport coincides with the period when the temperature gradient is large in the area. The seasonal cycle of Q_T^H, shown in Fig. 12, indicates that the offshore heat transport peaks in November, approaching 10 W m^{-2} in the southern Beaufort and Chukchi Seas. This offshore heat transport is likely to contribute to the delay of the seasonal freezing in the fall. We will like to emphasize here that the magnitude of this flux is not small when compared to 2–5 W m^{-2}, a commonly suggested value of oceanic heat flux from deeper and warmer water layer. Previous studies have shown that the solar radiation in the open-water areas provides a heat storage in the ocean mixed layer and plays an important role in the freezing–melting cycle of sea ice (Maykut and Perovich 1987). What has not been studied is how this stored heat is being redistributed by oceanic currents and thus affects the sea ice conditions elsewhere. A full investigation of this process will require a more sophisticated model that can properly handle ice–ocean interactions. This is clearly beyond the scope of this study.

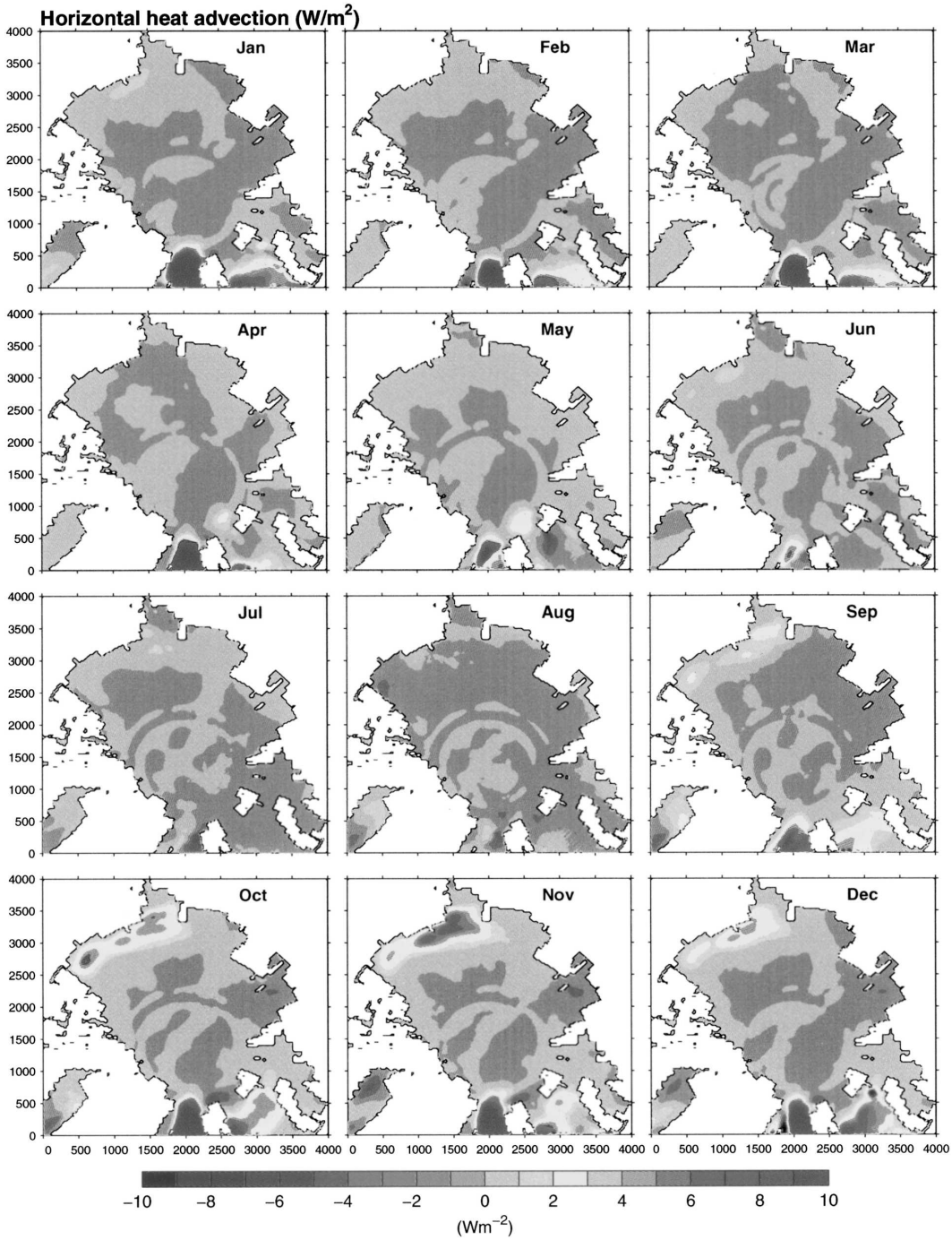

FIG. 12. The horizontal heat advection (W m^{-2}) due to the Ekman transport.

The magnitude of the upwelling/downwelling velocity w, as shown in Fig. 10, also peaks in the fall and early winter. Here, we calculate the heat flux to the mixed layer due to the upwelling by assuming the water to be upwelled comes from a depth of 30 m; that is, $T_{\text{sub}} = T_{30\text{m}}$. The mixed layer depth changes regionally and also seasonally, and so the use of 30-m depth to determine the temperature and salinity of the upwelling water in all regions cannot be vigorously justified. Data collected from two CTD stations in the Beaufort Sea in April of 1996 and 1997, however, did show that the mixed layer depth to be 20–30 m (Comiso et al. 2003).

The Ekman depth in the Arctic Ocean, as shown by Hunkins (1966), is about 20 m. So we decided to use 20 m as the depth of mixed layer and to use the next available depth (30 m) in the PHC data for setting the T and S of the subsurface water to be upwelled. The mixed layer is not well defined in the PHC data, which combined sparse observations made over a long period of time. The use of 30 m in this study will result in biases in regions where mixed layer depth is significantly different from 30 m. The heat advection is defined as

$$Q_T^W = C_p\rho(T_{\text{sub}} - T_{\text{mix}})M(w), \tag{8}$$

where M is the stepside function defined to be zero for w less than zero and to be w if w is greater than zero, the subscripts sub and mix refer to the subsurface and mixed layer, respectively. The use of stepside function is based on the fact that the mixed layer salinity and temperature are affected only by upwelling and not by downwelling (the subsurface property is affected by downwelling). This formulation has been widely used in the simple fixed-depth mixed layer model (e.g., Zebiak and Cane 1987). The distribution of $T_{\text{sub}} - T_{\text{mix}}$, shown in Fig. 8, indicates that the subsurface water is generally cooler than that in the mixed layer and thus the upwelling tends to result in a negative heat flux to the surface. This is indeed the case in our calculation as shown in Fig. 13. The cooling is mainly along the boundary mirroring the distribution of w (Fig. 10) in contrast to the broader and more offshore distribution of horizontal advection Q_T^H (Fig. 12). We must point out, however, that our calculation of heat flux in (8) is based on the open-ocean scenario, which becomes less valid along the boundary. In the coastal upwelling case, the water being upwelled usually originates from a bottom boundary layer that is separated from the surface Ekman layer. It is drawn from the shelf breaks, which is typically much deeper than that of Ekman-layer depth, to the coastline upward along the slope of shelves. The water tends to be considerably warmer than T_{sub} used in this study. In such cases, upwelling will result in a positive heat flux to the mixed layer along the coast. To calculate such flux requires a dynamical ocean model as shown by Carmack and Chapman (2003).

Similar to the heat flux calculation, we have also computed the salt flux to the surface mixed layer:

$$Q_S^H = D_E(u_E\partial S/\partial x + v_E\partial S/\partial y). \tag{9}$$

To compare the impact of freshwater flux on the salinity, we also define here the equivalent freshwater flux, $F_H = Q_S/S_0$, where $S_0 = 35$ psu. One unit of F_H would have the same effect on the salinity in a fixed depth mixed layer as one unit of freshwater flux does. In addition to the horizontal advection, we have also calculated the contribution from the vertical advection associated with upwelling,

$$Q_S^W = M(w)(S_{\text{sub}} - S_{\text{mix}}). \tag{10}$$

Likewise, we define an equivalent freshwater flux here; that is, $F_W = Q_S^W/S_0$.

Figure 14 shows the monthly distribution of F_H in the unit of cm month^{-1}. Along Fram Strait, the horizontal advection of salinity is positive in all months but is particularly strong in the fall and winter seasons. The Ekman transport is westward toward the coast along Greenland (Fig. 5) and is driven by the southward ice motion (Fig. 3) and wind (Fig. 2). Because the mixed layer water is saltier in the eastern side along Svalbard, the westward Ekman advection leads to the positive salt transport across the strait. Another area with prominent changes is in the southern Beaufort and Chukchi Seas. In the area off the coast between Barrow and Banks Island in the southern Beaufort Sea, the salinity advection is negative except in the month of August. The Ekman transport is directed offshore (Fig. 5) and the salinity is lowest along the coast (Fig. 6) except in July and August. This pattern of Ekman transport spreads the low-salinity coastal water and results in a negative F_H. The low salinity is mainly due to the runoff from the Mackenzie River. The equivalent freshwater flux reaches about 30 cm month^{-1} between October and December with an annual accumulation over 1 m. This represents a major freshwater source in the area. In the Chukchi Sea, however, the salinity advection is mostly positive. This positive advection, which is considerably stronger in the late fall around November and December (Fig. 14), is caused by the offshore Ekman transport (Fig. 5) of high-salinity Pacific water that enters the Arctic Ocean through Bering Strait (Fig. 6). The salinity advection in the Laptev Sea is also positive (Fig. 14) due to the advection of saltier Atlantic water inflowed through Barents Sea and Fram Strait (Figs. 5 and 6). The vertical advection due to the Ekman pumping is mainly along the boundary (Fig. 15) where the vertical velocity w is large (Fig. 10).

We will like to point out that the there is a discrepancy in our calculations of Ekman transport and T/S advections. The monthly Ekman transport and pumping rate, as discussed in section 3, are calculated by averaging the daily data of a 26-yr record into each month. The temperature and salinity fields, however, are from a long-term climatology. Ideally, one would like to calculate the monthly heat and salt advection

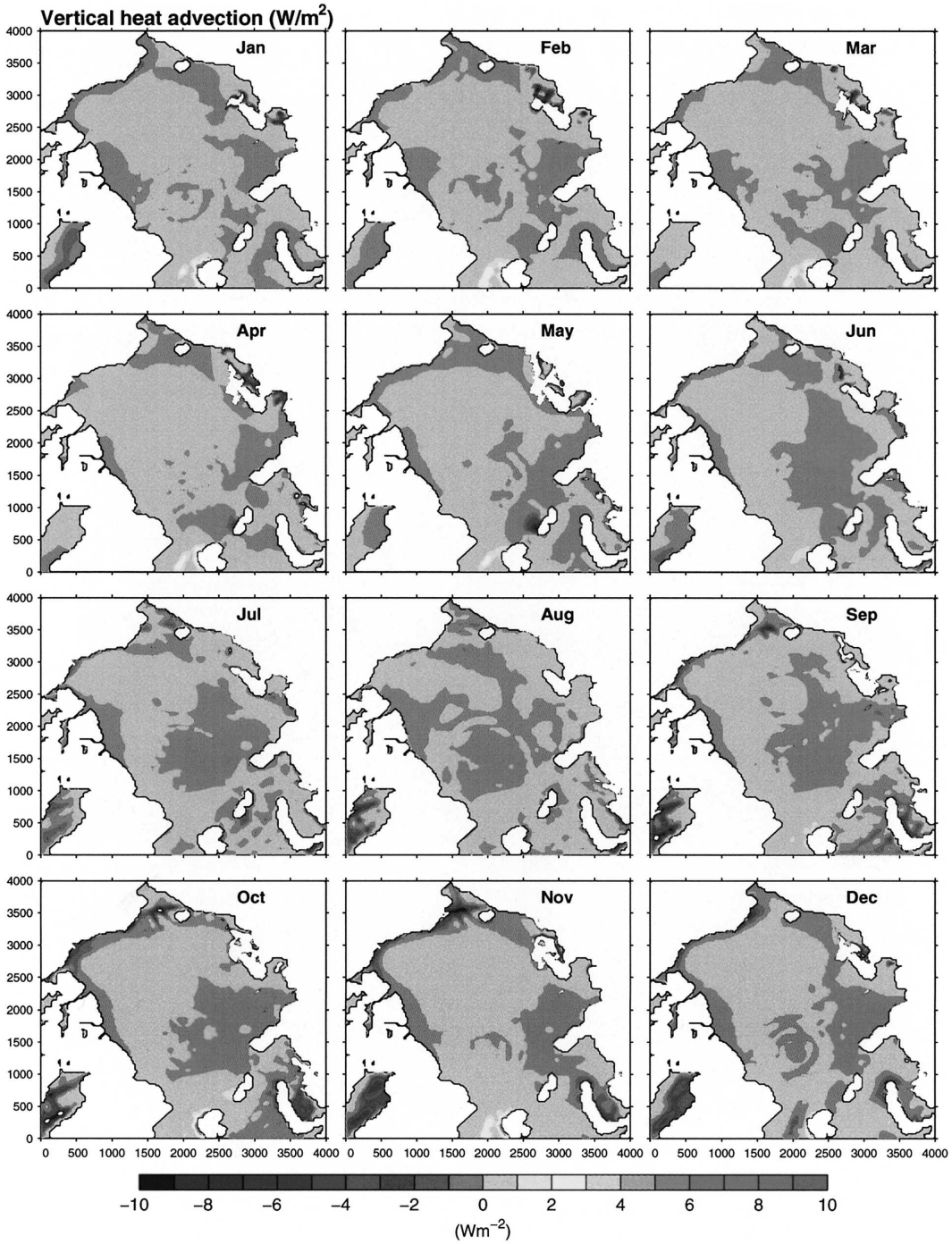

FIG. 13. The vertical heat advection (W m^{-2}) into the surface mixed layer because of upwelling.

from averaging the daily ones. But this is impossible since there is such daily dataset available for T and S.

5. Summary

In this study we have used observation-based data of SLP, geostrophic wind, sea ice motion, and sea ice concentration to calculate the daily Ekman transport and upwelling rate in the last 26 yr. The monthly climatologies of these two fields, which are derived based on the 26-yr daily data from 1978 to 2003, have been discussed in this paper. Overall, the Beaufort Sea and Fram Strait are two areas that have the greatest seasonal variations due to large seasonal variations of surface wind and ice

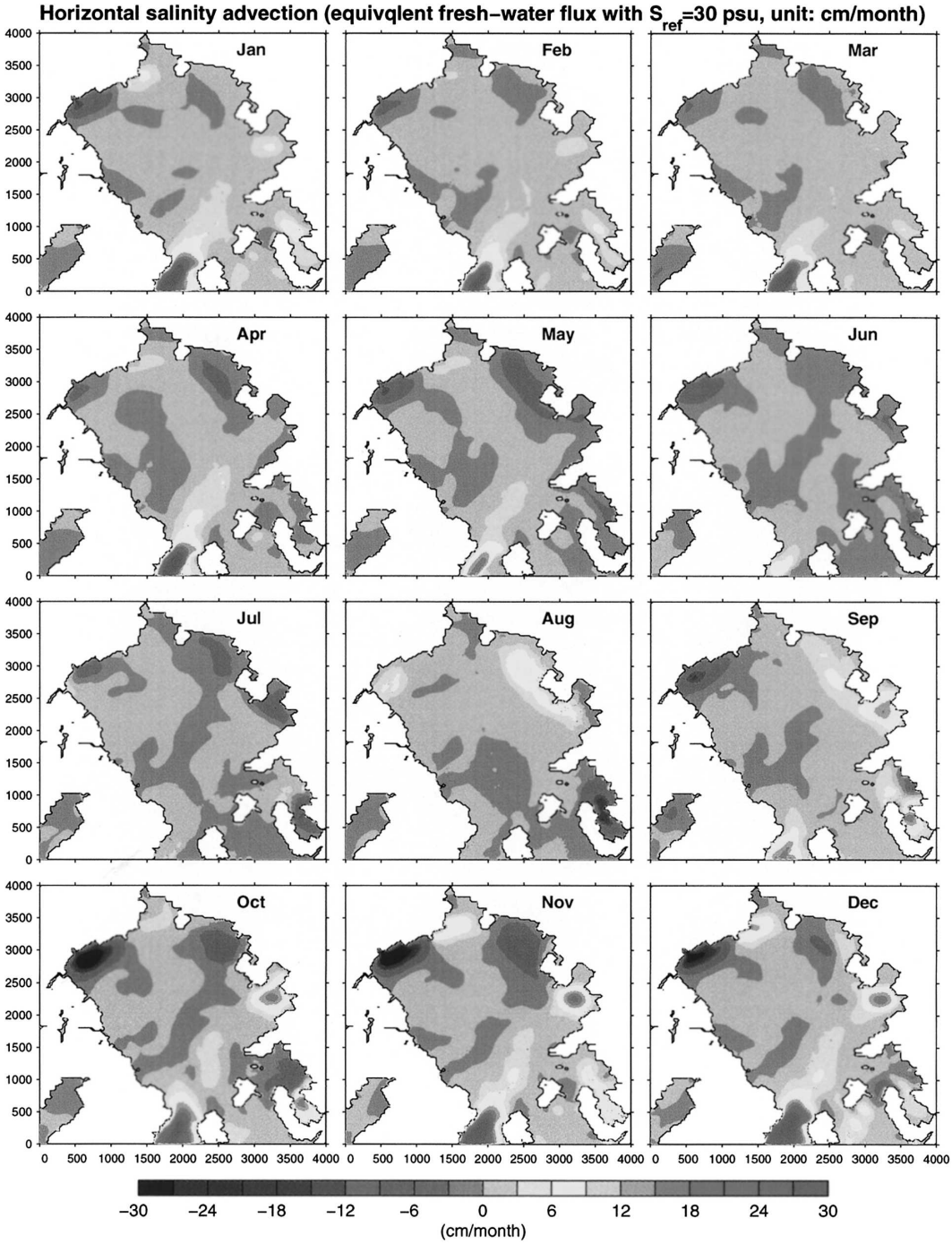

FIG. 14. The salinity advection (cm month^{-1}; equivalent freshwater advection relative to $S = 30$ psu) due to the Ekman transport.

motion. The maximum upwelling rate in this 26-yr climatology reaches as high as 15 cm day^{-1} in November and December in the southern Beaufort Sea. The heat advection associated with the Ekman transport is high in the Beaufort and Chukchi Seas. The maximum heat transport occurs in the fall when the offshore Ekman transport velocity is large and the mixed layer temperature gradient is also large. Into the winter months, however, the heat flux decreases rapidly even though the Ekman transport remains strong but the mixed layer

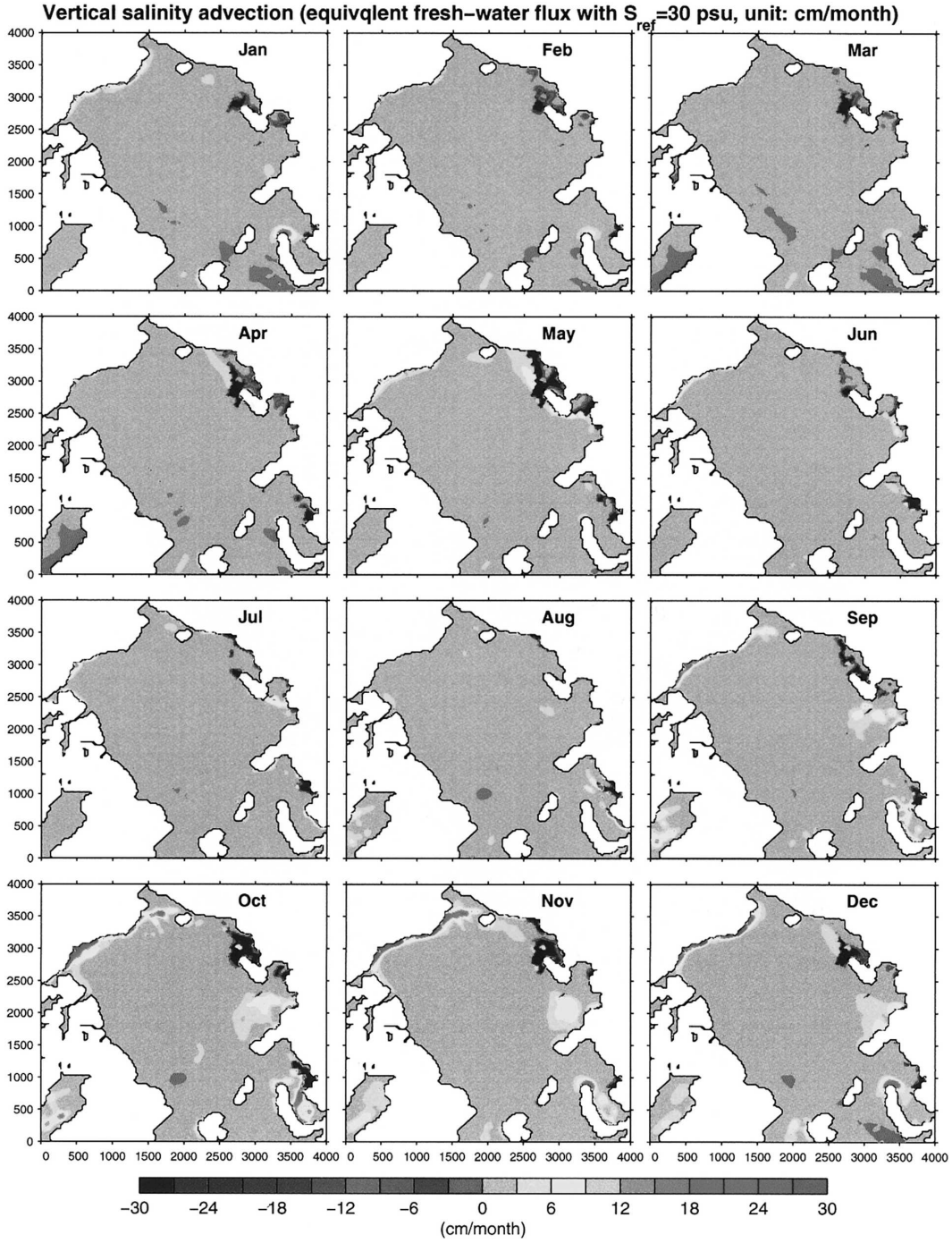

FIG. 15. The vertical salt flux (cm month^{-1}; equivalent freshwater flux relative to $S = 30$ psu) into the surface mixed layer due to the upwelling.

has been cooled to be nearly uniformly at the freezing point and thus the temperature gradient is small. The Ekman velocity also transports low-salinity coastal water and high-salinity Pacific Ocean water toward the Beaufort Sea in the fall and winter seasons. The freshwater flux associated with this advection is significant and comparable with other leading freshwater fluxes such as the summer melting of sea ice. The annual precipitation–evaporation rate in the Arctic is about 15 cm yr^{-1} according to Bromwich et al. (2000). The ampli-

tude of annual growth and melt rate of sea ice in central Arctic, according to a survey of various observational and modeling studies (Steele and Flato 2000), is 45–130 cm (growth) and 41–74 cm (melt).

While this study addresses only the seasonal cycle, we would like to point out that the Arctic Ocean is known to vary profoundly on the interannual and decadal time scales. The basin-scale circulation can even be reversed (Proshutinsky and Johnson 1997), a phenomenon that has rarely been reported elsewhere. The ice motion in the Beaufort Sea, for instance, can be opposite in the same month in two different years. So the Ekman velocity and pumping rate can be much greater in some years than the 25-yr averaged fields presented here. One would wonder whether the interannual and decadal variability of Ekman heat transport affects the sea ice condition in the regions. Another area for future study is the ice-edge upwelling (Buckley et al. 1979). Because of the discontinuity of surface stress across the ice edge, local upwelling or downwelling may occur. How this process affects the overall heat and salt flux remains to be studied.

Acknowledgments. This study has been supported by NASA Cryospheric Science Program (Grant NNG04GP34G) and by the NSF Office of Polar Program (Grant OPP0424074).

REFERENCES

Aagaard, K., L. K. Coachman, and E. Carmack, 1981: On the halocline of the Arctic Ocean. *Deep-Sea Res.,* **28A,** 529–545.

Bromwich, D. H., R. I. Cullather, and M. C. Serreze, 2000: Reanalyses depictions of the Arctic atmospheric moisture budget. *The Freshwater Budget of the Arctic Ocean,* E. L. Lewis et al., Eds., Kluwer Academic, 623 pp.

Buckley, J. R., T. Gammelsrod, J. A. Johannessen, O. M. Johannessen, and L. P. Roed, 1979: Upwelling: Oceanic structure at the edge of the Arctic ice pack in winter. *Science,* **203,** 165–167.

Carmack, E., and D. C. Chapman, 2003: Wind-driven shelf/basin exchange on an Arctic shelf: The joint roles of ice cover extent and shelf-break bathymetry. *Geophys. Res. Lett.,* **30,** 1778, doi:10.1029/2003GL017526.

Colony, R., and A. S. Thorndike, 1984: An estimate of the mean field of sea ice motion. *J. Geophys. Res.,* **89,** 10 623–10 629.

Comiso, J. C., 1995: Remote sensing of the Arctic. *Arctic Oceanography: Marginal Ice Zones and Continental Shelves, Coastal Estuarine Study,* W. Smith and J. Grebmeier, Eds., Amer. Geophys. Union, 1–50.

——, J. Yang, S. Honjo, and R. A. Krishfield, 2003: Detection of change in the Arctic using satellite and in situ data. *J. Geophys. Res.,* **108,** 3384, doi:10.1029/2002JC001347.

Dickson, R. R., and Coauthors, 2000: The Arctic Ocean response to the North Atlantic Oscillation. *J. Climate,* **13,** 2671–2696.

Fowler, C., 2003: Polar Pathfinder Daily 25km EASE-Grid Sea Ice Motion Vectors. National Snow and Ice Data Center, Boulder, CO. [Available online at http://nsidc.org.]

Gloerson, P., W. J. Campbell, D. J. Cavalieri, J. C. Comiso, C. L. Parkinson, and H. J. Zwally, 1992: Arctic and Antarctic sea ice, 1978-1987: Satellite passive-microwave observations and analysis. NASA Tech. Rep. SP-511, 290 pp.

Hakkinen, S., and A. Proshutinsky, 2004: Freshwater content variability in the Arctic Ocean. *J. Geophys. Res.,* **109,** C03051, doi:10.1029/2003JC001940.

Hellerman, S., and M. Rosenstein, 1983: Normal monthly wind stress over the World Ocean with error estimates. *J. Phys. Oceanogr.,* **13,** 1093–1104.

Hibler, W. D., III, 1980: A dynamic and thermodynamic sea ice model. *J. Phys. Oceanogr.,* **10,** 815–846.

Hunkins, K., 1966: Ekman drift currents in the Arctic Ocean. *Deep-Sea Res.,* **13,** 607–620.

Johnson, M. A., A. Y. Proshutinsky, and I. V. Polyakov, 1999: Atmospheric patterns forcing two regimes of Arctic circulation: A return to anticyclonic condition? *Geophys. Res. Lett.,* **26,** 1621–1624.

Kwok, R., A. Schweiger, D. A. Rothrock, S. Pang, and Ch. Kottmeier, 1998: Assessment of sea ice motion from sequential passive microwave observations with ERS and buoy ice motions. *J. Geophys. Res.,* **103** (C4), 8191–8213.

Maslowski, W., B. Newton, P. Schlosser, A. Semtner, and D. Martinson, 2000: Modeling recent climate variability in the Arctic Ocean. *Geophys. Res. Lett.,* **27,** 3743–3746.

Maykut, G. A., and N. Untersteiner, 1971: Some results from a time-dependent thermodynamic model of sea ice. *J. Geophys. Res.,* **76,** 1550–1575.

——, and D. K. Perovich, 1987: The role of shortwave radiation in the summer decay of sea ice cover. *J. Geophys. Res.,* **92,** 7032–7044.

——, and M. G. McPhee, 1995: Solar heating of the Arctic mixed layer. *J. Geophys. Res.,* **100,** 24 691–24 703.

Millero, F. J., G. Perron, and J. E. Desnoyers, 1973: Heat capacity of seawater solutions from 5 to 35°C and 0.5 to 22% chlorinity. *J. Geophys. Res.,* **78,** 4499–4507.

Parkinson, C., and D. J. Cavalieri, 1989: Arctic sea ice 1973-1987: Seasonal, regional and interannual variability. *J. Geophys. Res.,* **94,** 14 499–14 523.

——, ——, P. Gloersen, H. J. Zwally, and J. C. Comiso, 1999: Arctic sea ice extents, areas, and trends, 1978-1996. *J. Geophys. Res.,* **104,** 20 837–20 856.

Pond, S., and G. Pickard, 1983: *Introductory Dynamical Oceanography*. Pergamon Press, 329 pp.

Proshutinsky, A. Y., and M. A. Johnson, 1997: Two circulation regimes of the wind-driven Arctic Ocean. *J. Geophys. Res.,* **102,** 12 493–12 514.

——, and Coauthors, 2001: Multinational effort studies differences among Arctic Ocean models. *Eos, Trans. Amer. Geophys. Union,* **82,** 637–644.

Rigor, I., 2002: IABP drifting buoy, pressure, temperature, position, and interpolated ice velocity. Polar Science Center, Applied Physics Laboratory, University of Washington, Seattle, in association with NSIDC. Boulder, CO, National Snow and Ice Data Center. [Available online at http://nsidc.org.]

Rothrock, D. A., Y. Yu, and G. A. Maykut, 1999: Thinning of the Arctic sea ice cover. *Geophys. Res. Lett.,* **26,** 3469–3472.

Steele, M., and G. M. Flato, 2000: Sea ice growth, melt, and modeling: A survey. *The Freshwater Budget of the Arctic Ocean,* E. L. Lewis et al., Eds., Kluwer Academic, 623 pp.

——, R. Morley, and W. Ermold, 2001: PHC: A global hydrography with a high-quality Arctic Ocean. *J. Climate,* **14,** 2079–2087.

Thompson, D. W. J., and J. M. Wallace, 1998: The Arctic Oscillation signature in wintertime geopotential height and temperature fields. *Geophys. Res. Lett.,* **25,** 1297–1300.

Walsh, J. E., W. L. Chapman, and T. L. Shy, 1996: Recent decrease of sea level pressure in the central Arctic. *J. Climate,* **9,** 480–486.

Yang, J., and J. Comiso, 2005: An unexpected seasonal variability in the upper Beaufort Sea upper layer in 1996-98. *J. Geophys. Res.,* in press.

Zebiak, S. E., and M. A. Cane, 1987: A model of El Niño–Southern Oscillation. *Mon. Wea. Rev.,* **115,** 2262–2278.

Zhang, J., D. Rothrock, and M. Steele, 1998: Warming of the Arctic Ocean by a strengthened Atlantic inflow: Model results. *Geophys. Res. Lett.,* **25,** 1745–1748.

Zhang, Y. X., and E. C. Hunke, 2001: Recent Arctic change simulated with a coupled ice-ocean model. *J. Geophys. Res.,* **106,** 4369–4390.